JACS
JOURNAL OF THE AMERICAN CHEMICAL SOCIETY
pubs.acs.org/JACS
Article

Functional Dynamics of an Ancient Membrane-Bound Hydrogenase

Max E. Mühlbauer, Ana P. Gamiz-Hernandez, and Ville R. I. Kaila*

Cite This: J. Am. Chem. Soc. 2021, 143, 20873−20883
Read Online
ACCESS | Metrics & More | Article Recommendations | Supporting Information

ABSTRACT: The membrane-bound hydrogenase (Mbh) is a redox-driven Na^+/H^+ transporter that employs the energy from hydrogen gas (H_2) production to catalyze proton pumping and Na^+/H^+ exchange across cytoplasmic membranes of archaea. Despite a recently resolved structure of this ancient energy-transducing enzyme [Yu et al. *Cell* **2018**, *173*, 1636−1649], the molecular principles of its redox-driven ion-transport mechanism remain puzzling and of major interest for understanding bioenergetic principles of early cells. Here we use atomistic molecular dynamics (MD) simulations in combination with data clustering methods and quantum chemical calculations to probe principles underlying proton reduction as well as proton and sodium transport in Mbh from the hyperthermophilic archaeon *Pyrococcus furiosus*. We identify putative Na^+ binding sites and proton pathways leading across the membrane and to the NiFe-active center as well as conformational changes that regulate ion uptake. We suggest that Na^+ binding and protonation changes at a putative ion-binding site couple to proton transfer across the antiporter-like MbhH subunit by modulating the conformational state of a conserved ion pair at the subunit interface. Our findings illustrate conserved coupling principles within the complex I superfamily and provide functional insight into archaeal energy transduction mechanisms.

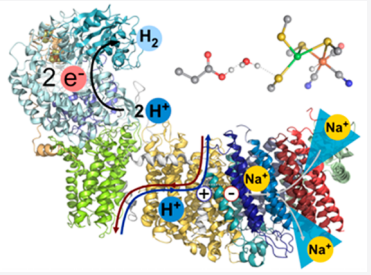

INTRODUCTION

The membrane-bound hydrogenase (Mbh) is a primordial enzyme that powers energy transduction in the thermophilic archaeon *Pyrococcus furiosus*.[1,2] Mbh catalyzes ferredoxin (Fd)-driven ($E_{m,7}$ = −450 mV, redox midpoint potential at pH = 7) hydrogen gas production ($E_{m,7}$ = −420 mV)[1−4] and employs the small thermodynamic driving force ($\Delta G \sim -60$ mV) for proton pumping and Na^+/H^+ exchange.[3,4] The sodium motive force (smf) generated across the archaeal membrane powers subsequent Na^+-driven ATP synthesis.[5]

Mbh is a 14-subunit enzyme complex[1,2,6] comprising a hydrophilic domain, responsible for electron transfer and H_2 production, and a membrane domain driving Na^+/H^+ transport, with the recently resolved cryoEM structure revealing key features of its molecular architecture[1] (cf. also ref 7). Mbh is a predecessor of the modern complex I superfamily,[1,7,11] which catalyzes NADH- or Fd-driven quinone (Q) reduction and couples the much larger ($\Delta G \sim -800$ to -1200 mV) driving force to proton pumping across the membrane domain. Despite intensive work in recent years,[8−12] the molecular principles of the fascinating energy transduction mechanism employed by this superfamily remain unsolved.

The catalytic cycle of Mbh is initiated by association of the reduced Fd to the positively charged MbhN at the top of the hydrophilic domain, comprising subunits MbhI-MbhL and MbhN (Figure 1). The electrons are transferred from Fd via three tetranuclear iron−sulfur (FeS) centers to the NiFe core of MbhL, responsible for the proton reduction.[1] The binuclear NiFe catalytic center is coordinated by four cysteine residues ($Cys68_L$, $Cys71_L$, $Cys374_L$, $Cys377_L$), in addition to two CN^-

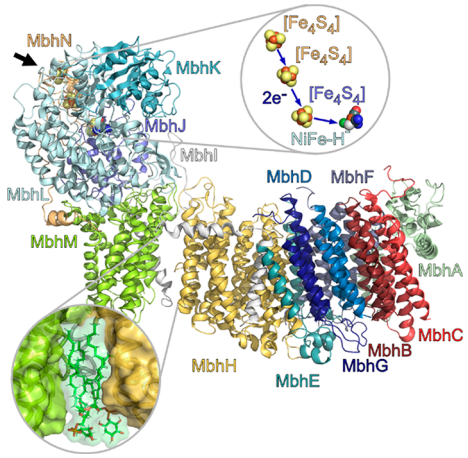

Figure 1. Structure and function of Mbh. Ferredoxin docks to MbhN (position indicated by black arrow) and transfers electrons via the FeS centers to the NiFe active site (inset), where protons are reduced to hydrogen gas ($2H^+ + 2e^- \rightarrow H_2$). Proton transport and Na^+/H^+ exchange could take place in MbhM/MbhH and MbhA-G, respectively (see the main text). A lipid gap with modeled phosphatidylinositol is shown in the bottom inset.

Received: September 3, 2021
Published: November 30, 2021

https://doi.org/10.1021/jacs.1c09356
J. Am. Chem. Soc. 2021, 143, 20873−20883

and a CO ligand, and closely related to soluble NiFe-hydrogenases.[1,13] The membrane domain of Mbh comprises eight subunits responsible for ion transport (Figure 1). Based on mutagenesis and structural studies of the related Mrp (multiple-resistance and pH adaption) transporters,[1,14,15] the Na^+/H^+ exchange was suggested to take place in MbhB/C/D/G (MrpF/G/A_{nt}/C in Mrps).[14,15] Together with MbhA/F/G (Figure 1), these subunits located on the terminal edge of Mbh establish a bundle of 3 × 4 transmembrane (TM) helices—a symmetric motif common in many antiporters.[8,9,11,14,15]

MbhH is related to the proton pumping NuoN module of complex I (*E. coli* nomenclature; Nqo14/ND2 in other species), but it is rotated by 180° in the membrane relative to the former (Figure 1). This antiporter-like subunit comprises two symmetry-related TM-helix bundles with one broken helix each, buried charged residues, and a conserved ion pair. These features form functional elements for water-mediated proton pumping in complex I[16−24] and could have a similar function in Mbh. MbhH is further clamped by an amphipathic transverse helix of MbhI that could secure tight electrostatic interaction between the subunits.[8]

MbhG and MbhD+E are related to NuoK/J (Nqo11/10, ND4L/ND6)—subunits that are also most likely involved in proton transport in complex I.[8,9,16,18,20−24] However, in contrast to the latter where they reside close to the interface between the hydrophilic and membrane domains, these subunits are located in the middle of the membrane domain in Mbh (Figure 1). MbhG/D/E could catalyze Na^+/H^+ transport, although the molecular principles remain debated. Yu et al.[1] suggested that MbhC is responsible for Na^+ transport, while proton transfer was suggested to occur in MbhH and MbhD/G. In contrast, Steiner and Sazanov[15] resolved sodium ions in Mrp subunits homologous to MbhD (N-terminal part of MrpA) and MbhG (MrpC). A sodium pathway was also suggested to reside in MbhA (MrpE), with a putative input channel from the negatively charged side (cytoplasmic side) in MbhA and an output site to the positively charged side (periplasmic side) of the membrane at the MbhG/F/H interface (Figure 1). Sodium ions have also been suggested to enter MbhH (MrpD) and exit to the periplasmic side at MbhF/G/H.[14]

The membrane-bound MbhM (related to NuoH/Nqo8/ND1 of complex I) forms an "ankle" region at the interface of the hydrophilic and membrane domain. This region has a special functional role in complex I,[18,23−25] whereas a large, ca. 10 Å wide cleft is observed in the cryoEM structure at the MbhM/MbhH interface (Figure 1, bottom inset).[1] The structure also revealed conserved loop regions within MbhM (NuoH/Nqo8), MbhI (N-terminal part of NuoA/Nqo7), and MbhL (NuoD/Nqo4), which undergo conformational changes in complex I.[20,23,26,27]

To shed light on the elusive ion transport mechanism of Mbh, we probe here the coupling and dynamics between the redox and proton pumping domains and the sodium/proton exchange domain in the membrane-bound hydrogenase from *P. furiosus*[1] by combining classical molecular dynamics simulations and data clustering methods, with quantum chemical calculations. Our findings illustrate detailed hydration dynamics, putative sodium and proton binding sites, and possible locations of the proton channels. We also present a mechanistic model that could explain how the coupling between redox-driven proton reduction, proton pumping, and ion transport is achieved.

RESULTS

Global Dynamics and Proton Wires Leading to the Active Site. To gain insight into the functional dynamics of Mbh, we performed 8 μs of MD simulations of the solvated 14-subunit enzyme modeled in a phosphatidylinositol (PI) membrane, which is abundant in *P. furiosus*,[28] and explored the effects of modeling key residues in different protonation states (Tables S1 and S2). Mbh remains structurally stable during the MD simulations, with an overall root-mean-square deviation (RMSD) of <4 Å relative to the refined cryoEM structure (Figure S1A). The protein shows a high flexibility toward the cytoplasmic side surface of MbhA/B/C and the upper part of the hydrophilic domain (Figure S1B).

The conserved loops connecting the active site and a charged funnel in MbhM are also highly flexible, particularly the long MbhI loop, which we modeled *in silico* based on the experimentally resolved backbone coordinates. We note that the dynamics projected from the MD simulations are in good overall agreement with *B*-factors extracted from the cryoEM maps (Figure S1B), supporting that the simulations capture the global dynamics of the protein.

To probe possible H^+ and Na^+ transfer pathways, we next analyzed buried water networks formed during the MD simulations. The dry cryoEM structure reaches a highly hydrated state within 100 ns of the MD simulations, where a few hundred water molecules form transient interactions within the hydrophilic domain as well as buried parts of the membrane domain (Figure 2A,B and Figure S2). The water

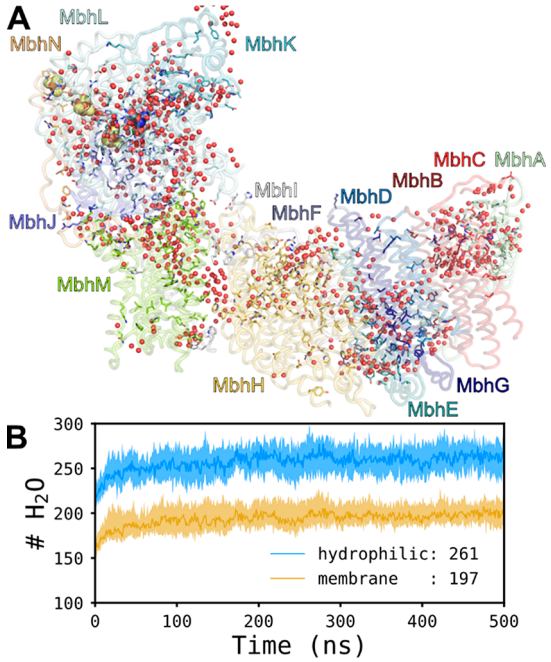

Figure 2. Global hydration dynamics of Mbh. (A) Conserved residues (see the Methods section) within the complex I superfamily are shown in stick representation and buried water molecules from MD simulations within 6 Å of these residues as red spheres. (B) Around 200−250 water molecules associate with the hydrophilic (MbhI-N, blue) and the membrane domains (MbhA-H, yellow) of Mbh during MD simulations. The plot shows the median over 16 independent simulations (8 μs in total) for each time point, with 25 and 75 percentiles, represented by the shaded areas. Hydration dynamics for individual subunits are reported in Figure S2.

https://doi.org/10.1021/jacs.1c09356
J. Am. Chem. Soc. 2021, 143, 20873−20883

wires connecting the cytoplasmic side with the NiFe site could conduct protons for H_2 production. On the basis of clustering analysis (see the Methods section), we observe four possible proton channels (see definition in the Supporting Information), comprising several charged residues and water molecules, leading to $Glu21_L$ (Figure 3A,B, Figure 4, and

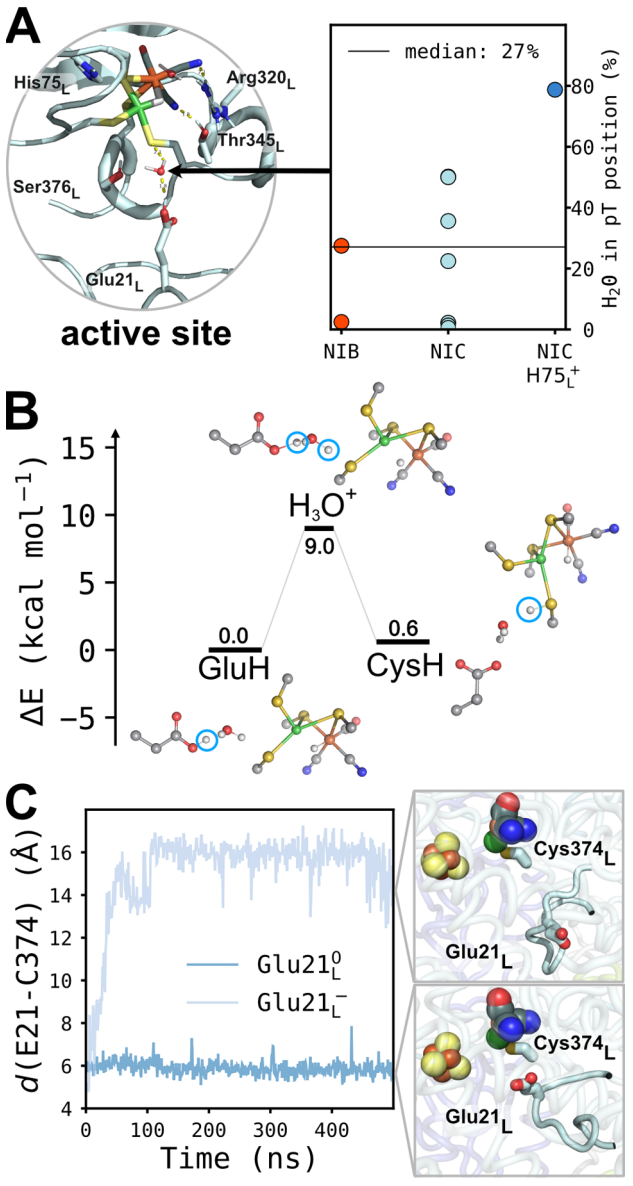

Figure 3. Hydration and protonation dynamics of the Mbh active site. (A) The NiFe cluster is stabilized by conserved contacts to surrounding residues. $Glu21_L$ on the $\beta1-\beta2$ loop is bridged to $Cys374_L$ by a water molecule in up to 85% of the MD simulation time depending on the state (NIB: OH^- ligand; NIC: H^- ligand; NIC $H75^+$: NIC with cationic $His75_L$). (B) DFT calculations suggest that water-mediated proton transfer from $Glu21_L$ to $Cys374_L$ is energetically and kinetically feasible. Only the chemically active atoms are shown. See Figure S4, Table S5, and Movie S1 for further details. (C) $Glu21_L$ flips away from the active site upon deprotonation.

Figure S3A), a highly conserved residue within hydrogenases[13] located on the $\beta1-\beta2$ loop next to the NiFe site. The active site $Cys374_L$ is further bridged by a water molecule to $Glu21_L$, particularly when $His75_L$ is modeled in a protonated state (Figure 3A). Interestingly, the neighboring $Glu20_L$ corresponds to the quinone-coordinating active site histidine ($His38_{Nqo4}$ in *T. thermophilus*) in complex I and is conformationally flexible.[1,7−12,18] Water influx occurs at the interface between MbhL and MbhM formed by the lower edge of the β-sheet in MbhL (around 25%; median over all simulations, Figure 4 and Figure S3B). Channels also form along the interface of the $\beta1-\beta2$ and MbhI loops (25%, Figure 4 and Figure S3B) and at the MbhL/MbhJ interface (34%, Figure 4 and Figure S3B). A cleft between MbhM and MbhH (12%) also weakly contributes to the overall water influx into the NiFe-site (Figure 4 and Figure S3B), similar to the E-channel in complex I.[8,18,20−25] These channels, particularly around the $\beta1-\beta2$ loop, comprise functionally important motifs in the canonical complex I,[8,11] thus also supporting their relevance in Mbh.

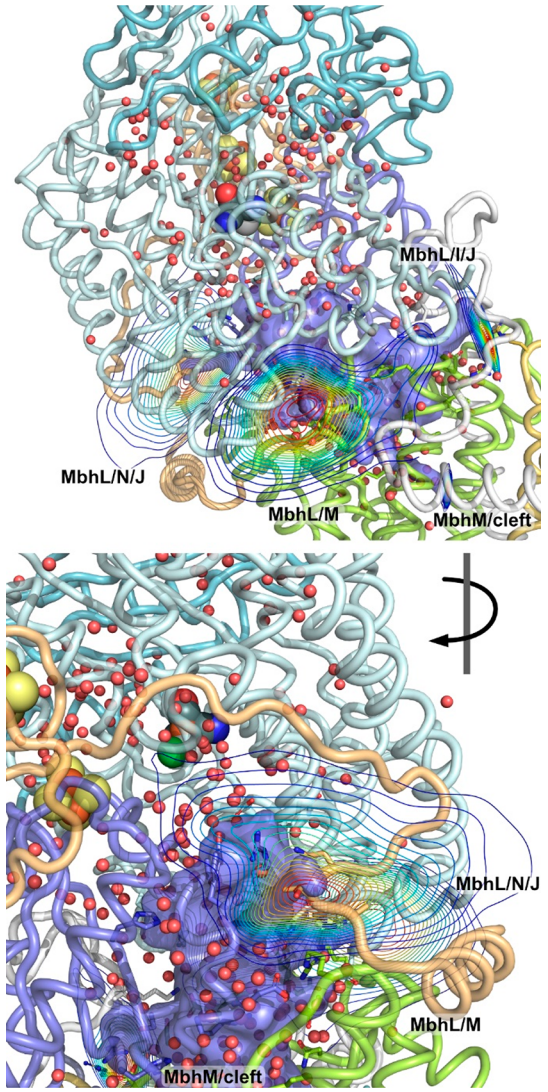

Figure 4. Water clusters leading to the cytoplasmic bulk and the cleft between MbhH and MbhM could allow for reprotonation of $Glu21_L$ from the bulk. The clusters are present in all simulations, but the number of water molecules varies depending on the protonation states. The figure shows centroid pathways based on cluster analysis (see the Methods section).

Interestingly, when $Glu21_L$ is modeled in its protonated state, as predicted by our electrostatic calculations (see the Methods section), the residue forms a water-mediated contact with $Cys374_L$ of the NiFe site (Figure 3A,C). In contrast, upon

https://doi.org/10.1021/jacs.1c09356
J. Am. Chem. Soc. 2021, 143, 20873−20883

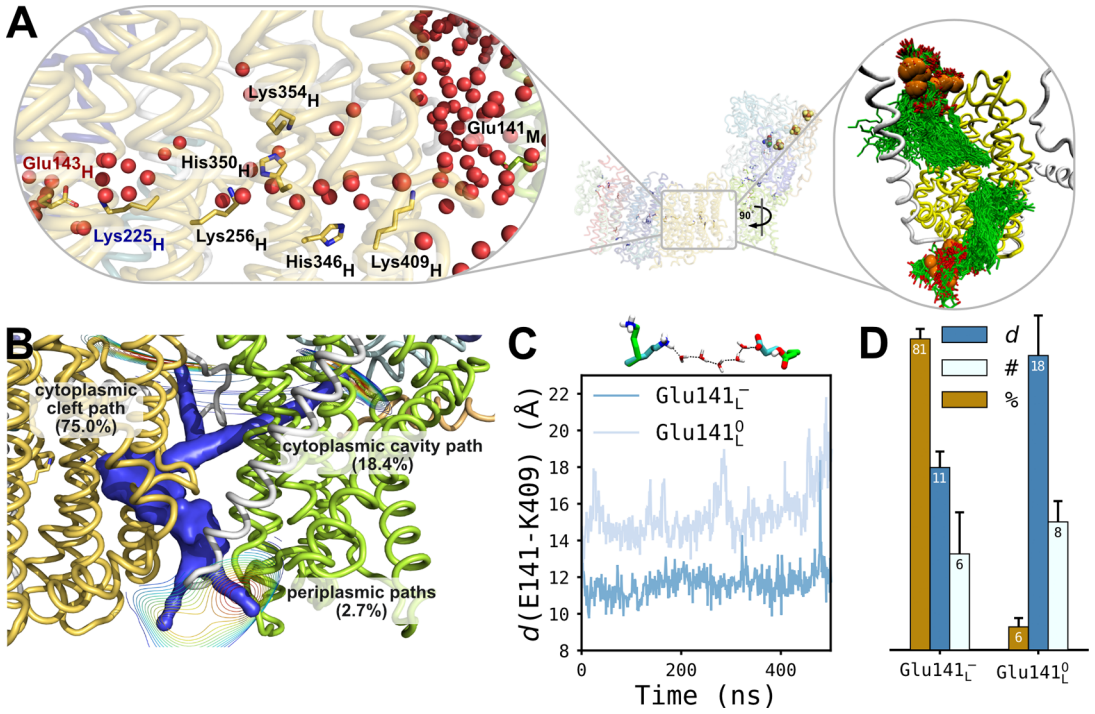

Figure 5. Structure and dynamics of MbhH. (A) Left inset: water molecules establish a hydrogen-bonded proton array between the cytoplasmic bulk and the hydrophilic axis, comprising histidine and lysine residues and leading to $Lys256_H$. The figure shows the last snapshot (500 ns) from simulation S3 (Table S1). Right inset: lipid binding sites on the cytoplasmic and periplasmic sides of the membrane showing the 20 most probable binding poses from eight independent simulations, as determined by pyLipid (see Supporting Information, Methods). (B) Water pathways based on clustering analysis of 8 μs MD data (see the Methods section). Three water inlet clusters serve as water conduits to the hydrophilic axis in MbhH: (I) from the cytoplasm via the lipid cleft (contribution 75%), (II) from the cytoplasmic side via the E-channel homologue in MbhM (18.4%), and (III) from the periplasmic side by a water wire between TM1/2 of MbhI and TM2/3 of MbhM via the broken helix TM12 of MbhH (2.7%). (C) Distances between $Glu141_M$ and $Lys409_H$ across the lipid filled cleft during MD simulations. Protonation of $Glu141_M$ increases the distances to $Lys409_H$. See Figure S9 for distance distribution in all simulations. The inset shows the shortest water-mediated pathway between the two residues in the deprotonated state (cyan sticks) and the lack of connectivity in the protonated state (green sticks). (D) Protonation of $Glu141_M$ increases the distance to $Lys409_H$ (dark blue, in Å) and disrupts the hydrogen-bonding (HB) connectivity, as shown by the probability of the stable HB wire between the two residues (in tan) and the number of HBs along the shortest path (in light blue).

deprotonation, $Glu21_L$ flips away from the NiFe site toward the hydrated channels leading to the cytoplasmic bulk phase at the MbhM/MbhL interface (Figure 3C and Figure S3).

To probe whether $Glu21_L$ could act as a proton donor for $Cys374_L$, we performed quantum chemical density functional theory (DFT) calculations (Figure 3B), which allowed us to address the reaction energetics along key steps of the NiFe catalytic cycle (see the Methods section, Figure S4). The water-mediated proton transfer from $Glu21_L$ to $Cys374_L$ has a reaction barrier of around 9 kcal mol^{-1}, and the two states are nearly isoenergetic by ΔE = +0.6 kcal mol^{-1} in the Ni^{II}/Fe^{II} state (Figure 3B, Table S5, and Movie S1).

These findings suggest that the proton uptake is kinetically accessible on physiologically relevant time scales along the conserved $Glu21_L/Cys374_L$ pathway (Figure 3B), residues that may also be functionally important in canonical hydrogenases.[29,30,35] Formation of the protonated $Cys374_L$ leads to an elongation of the Ni−$Cys374_L$ bond (Figure 3B and Figure S3), which in turn opens up the contact for the proton to the H^- bound between the Ni and the Fe. This could lead to the formation of the H_2 species in a process, enabled by a subtle (130° rotation of the Cys−H bond (Figure 3B, Figure S4, Table S5, and Movie S1; cf. also refs 29 and 30). We note that the conformation of $Arg320_L$, which forms contacts with both the NiFe center and $Asp372_L$, strongly influences the energetics of these reaction steps, and samples both inward and outward conformations in the MD simulations (Figure S9D), while the conserved salt-bridge to $Asp372_L$ remains intact. On the basis of the water network analysis and DFT calculations, we suggest that at least one proton could be transferred from the cytoplasmic bulk phase to the NiFe center for the H_2 production via $Glu21_L$, $Cys374_L$, and the water channels formed around the $\beta1-\beta2$ loop.

Functional Hydration of the Mbh Membrane Domain. The membrane domain of Mbh undergoes a significant hydration change during the MD simulations, in which around 200 water molecules establish pathways that could enable both proton and Na^+ transport across the membrane (Figure 2A,B and Figure S2). We observe a hydration site from the cytoplasmic side at the large cleft between MbhH and MbhM (Figure S5A,B). These water molecules form hydrogen-bonded arrays toward the central axis of MbhH connecting $Lys256_H$ with $His346_H$, $His350_H$, and $Lys354_H$. This pathway leads to the cytoplasmic bulk between MbhH and MbhM via $Lys409_H$ (Figure 5A) and accounts for a significant portion of the water influx toward MbhH. The same site was recently suggested to support Na^+ transport in the related Mrps,[14] although the chain of three conserved lysine residues along the pathway is expected to electrostatically disfavor Na^+ transport.

A transient water chain also connects $Glu141_M$ with $Lys409_H$ across the nonpolar lipid-filled cleft (Figure 5C,D). However, these residues are ca. 10−12 Å apart when $Glu141_M$

https://doi.org/10.1021/jacs.1c09356
J. Am. Chem. Soc. 2021, 143, 20873−20883

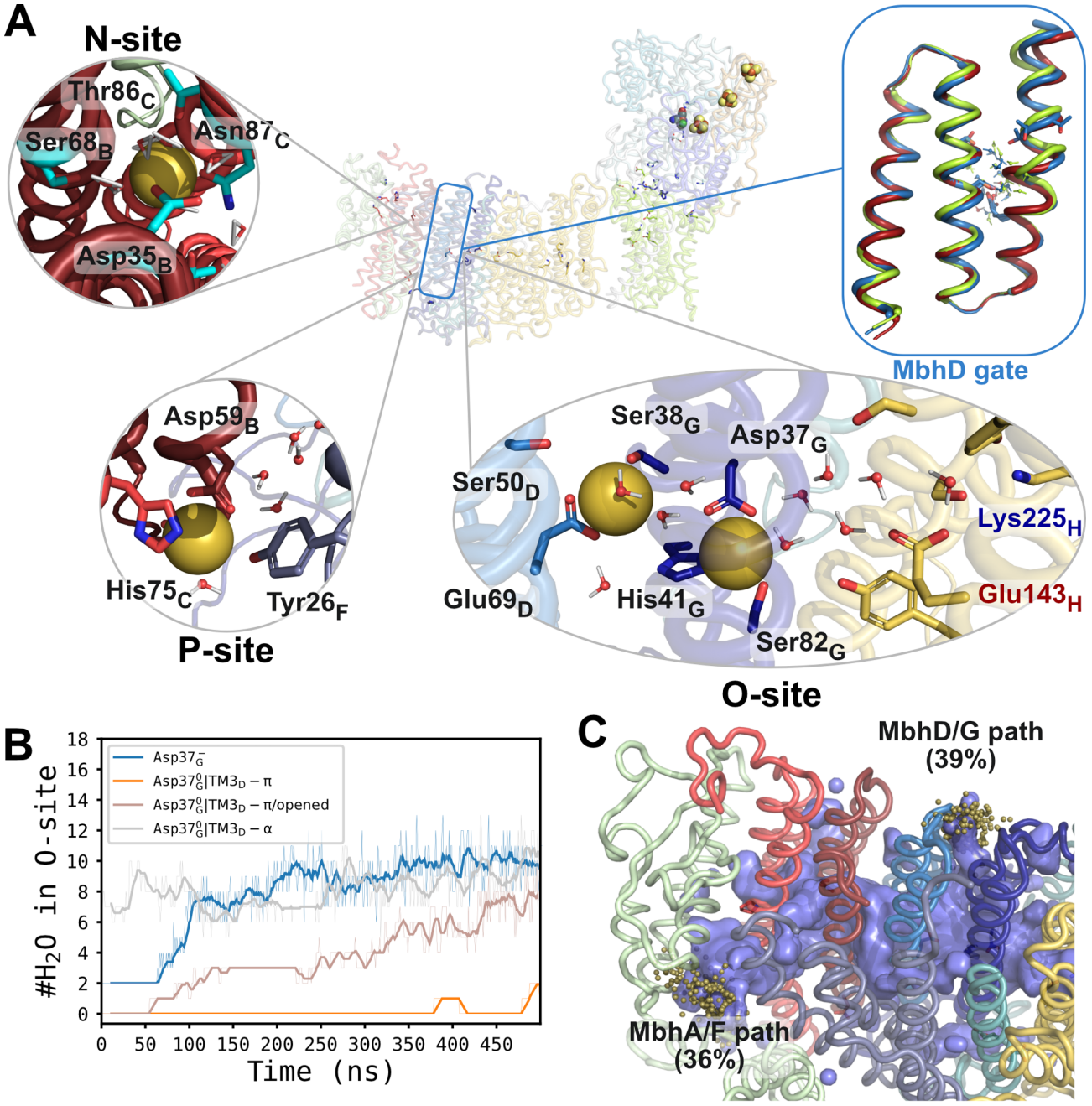

Figure 6. Na^+/H^+ transport in MbhA-G. (A) Putative sodium binding sites and functional motifs in Mbh based on MD simulations. Insets: the N-site at MbhA/C, here with a bound Na^+, is accessible from the cytoplasmic bulk; O-site in MbhG with two modeled Na^+ ions; P-site, which spontaneously binds bulk Na^+ ions during most MD simulations; and a putative conformational gate at TM2/TM3 of MbhD modulating ion transport between the N- and O-sites. (B) Hydration of the O-site in different protonation and conformational states. $Asp37_G$ deprotonation (blue) and conformational changes in the MbhD gate (brown) favor hydration of the O-site. Hydration in the closed-gate conformation (π-bulge form) is low (orange), whereas biasing toward α-helical conformation (gray) increases the hydration levels (see Figure S6). (C) O-site hydration in MD simulations. Influx via MbhD/G and MbhA/F accounts for ca. 75% of the observed water molecules in the region. The MbhA/F pathway is connected from the N-site via the MbhD gate to the O-site. Inlets from pathway cluster analysis are shown as spheres, and areas with volumes of greater than median hydration are depicted as surface.

is modeled in a deprotonated state and ca. 18 Å upon protonation of the latter, rendering proton exchange between the residues unlikely, especially since no titratable groups stabilize the long hydrogen-bonding wire.

Three to four PI lipids bind to the cleft region (Figure 5A), sealing the MbhH/MbhM gap from the periplasmic side and the horizontal gap at the MbhH/MbhM interface near the broken helix TM12 (Figure 5A). This observation is consistent with the blurred density around the region in the cryoEM map.[1]

Our simulations also indicate that binding of at least one additional lipid from the cytoplasmic side is sterically possible, which could block the proton transfer across the MbhM/MbhH interface (Figure S3D).

We observe another water influx site from the periplasmic side that reaches $Lys409_H$ between MbhI and MbhH (TM12),

https://doi.org/10.1021/jacs.1c09356
J. Am. Chem. Soc. 2021, 143, 20873−20883

with many conserved polar residues lining up along the pathway (Figure 5A,B). This cluster, which has an overall occupancy of around 5%, is not present in all simulations (Figure S3B), but it could nevertheless be functionally relevant. Although no water molecules enter the hydrophilic axis of MbhH via TM7, we observe a partial pathway leading to the cytoplasmic side around $Lys256_H$, $His350_H$, $Lys354_H$, and water molecules (Figure 5B). These findings thus indicate that a canonical S-shaped pathway, analogous to those observed in complex I,[20,21,23,24] could also establish a proton pathway in MbhH.

Residues along the lateral proton transfer wire in MbhH strongly interact with the conserved $Lys225_H$/$Glu143_H$ ion pair at the interface of MbhH and a putative Na^+-binding MbhG/D (see below), but the two regions do not exchange water molecules (Figure 5A). The conformation of this ion pair could modulate the proton transfer barrier along the lateral pathway in MbhH, and vice versa, similar to what has been observed in complex I (see below).[8,16,19,20,36]

This ion pair also forms strong electrostatic interactions with a charged cluster in MbhG/D, comprising $Asp37_G$, $His41_G$, and $Glu69_D$ residues that bind Na^+ in Mrp (Figure 6A, see below).[15] This region, called here the "O-site" (for the occluded Na^+ binding site) together with the ion pair, is hydrated from the cytoplasmic side of the membrane during our simulations and could form key elements enabling proton-coupled Na^+ transport.

Hydration Dynamics of the Putative Na^+-Binding Site. We find that hydration of the putative O-site occurs via two main pathways, which account for >75% of the water molecules observed in this region. The major channel leads from the cytoplasmic side at the MbhA/MbhF interface and is established around a kink region at $Pro88_C$ of the broken helix TM3 of MbhC (Figure 6A). The water molecules flow in via a cluster of conserved polar residues in MbhB and MbhC ($Thr39_B$/$Thr42_C$ and $Asp35_B$/$Asn38_B$/$Thr86_C$) that could form a primary Na^+ binding site (Figure 6A), here called the "N-site" (for negatively charged side Na^+-binding site). Interestingly, a similar motif establishes a Na^+ binding site in the unrelated light-triggered Na^+-pump KR2.[32] In the related Mrps, a Na^+ pathway was recently suggested to also involve a Thr/Asn cluster,[15] but leading via $His137_A$ toward the proposed N-site.[15] In our simulations, the latter pathway remains sealed from water molecules, whereas in Mrps, two detached TM-helices (in the subunit homologous to MbhA) could open up this channel.

To further probe the principles underlying sodium binding, we placed a Na^+ ion around the N-site in MbhB/MbhC. In these simulations, the Na^+ rapidly finds a binding pose that is stabilized by $Asp35_B$, $Asn87_B$, $Ser68_B$, $Thr86_C$, and water molecules (Figure 6A and Figure S5). Mutations of the homologous residues in Mrps block Na^+ transport activity, thus further supporting the functional relevance of this site.[14]

Water molecules also enter from the cytoplasmic side between MbhD and MbhG close to $Lys23_G$ and $Lys28_G$ and lead further to the O-site that could support proton transfer across this region. The MbhD/G pathway is favored in simulations, where $Asp37_G$ is modeled in a deprotonated (anionic) state. We note, however, that the high positive charge around this region is unlikely to support Na^+ transport (cf. ref 14), unless protonation changes are involved (cf. also ref 1).

MbhD Regulates Ion Transport to the Na^+/H^+ Coupling Site. The conformation of the π-bulge in TM3 of MbhD (residues 71−79) correlates with the overall water influx toward the putative Na^+/H^+ coupling site in MbhD/G (Figure 6B). In the hydrated state, the π-bulge moves toward MbhF and opens up a gap between TM2 and TM3 of MbhD (Figure 6B). This leads to an increase in the hydration level by a factor of 2 (Figure 6B and Figure S6B), whereas in the dry state, the TM2 and TM3 helices remain in close contact and prevent water diffusion across the site (Figure 6A).

The conformational state of the TM3 helix of ND3 in the canonical complex I was recently suggested to regulate proton transfer during the active-to-deactive transition and possibly during turnover.[23−27] More specifically, the α-helical form, present in the active state of complex I, favors well-wired proton pathways, whereas the π-bulge, observed in the deactive state, could block proton transfer.[24] Interestingly, the homologous TM3 of MrpA is captured in an α-helical form,[15] suggesting that conformational transitions between a π-bulge and α-helix could also be involved in Mbh.

To further probe how such conformational transitions affect the hydration dynamics in Mbh, we perturbed TM3 of MbhD to form an α-helix during the MD simulations (see Supporting Information Methods). The modeled α-helix remains dynamically stable for 0.5 μs during unrestrained MD simulations (Figure S7) and results in rapid hydration of the sodium cavity from the cytoplasmic side via MbhA (Figure 6B,C). In stark contrast, in simulations where TM3 forms a π-bulge, the region becomes 90% less hydrated (Figure 6B). These findings suggest that TM3 of MbhD could act as a gate that controls water and Na^+ exchange between the proposed N- and O-binding sites.

Sodium Binding at the P-Site. We observe spontaneous sodium binding in nearly all MD simulations at the periplasmic side surface in a cavity formed by MbhB, MbhC, and MbhF (cf. also ref 1). The Na^+ binds to the conserved $Asp59_B$, $Tyr26_F$, and $His75_C$ or, in a few simulations, to the nearby loop of MbhA. Both binding modes remain highly stable throughout the 0.5 μs simulations (Figure S5G), with rapid water exchange with the bulk. However, in contrast to the N-site at the MbhB/C interface, we do not observe pathways leading toward the interior of Mbh or to the O-site, located ca. 18 Å away. However, Na^+ transport to/from the P-site could be achieved by conformational switching into an alternate access state,[37] possibly supported by the structurally similar TM motifs also found in other transporter proteins.[38]

Sodium Transport between Binding Sites. To probe the Na^+ transport mechanism between the putative N- and O-sites, we placed sodium ions at the respective sites or at the MbhC/MbhD interface. The Na^+ ions remain tightly bound at the N- or O-sites on 0.5 μs time scales (Figure 7A), but at the interface region, the Na^+ interacts with TM2 and TM3 of MbhD for ca. 0.5 μs, after which it moves to the O-site to a position that closely resembles the binding mode in Mrp (Figure 7B and Figure S10).[15] These findings support that the MbhD gate could be involved in Na^+ transport in Mbh.

We also probed the reverse Na^+ transport direction by placing Na^+ ions at both sides of $His41_G$, as experimentally resolved for Mrp.[15] When the carboxylates are modeled in their deprotonated states, the Na^+ ions remain strongly bound at the O-site (Figures 6A and 7A), whereas upon protonation of $Asp37_G$ and $Glu69_D$, the Na^+ moves to the N-site within 50 ns (Figure 7A). The Na^+ diffusion leads to a subtle

https://doi.org/10.1021/jacs.1c09356
J. Am. Chem. Soc. 2021, 143, 20873−20883

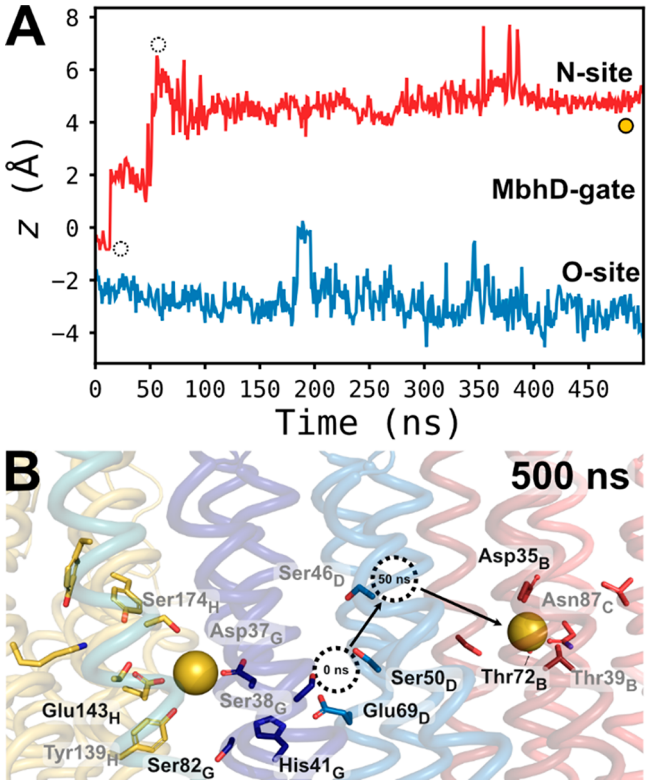

Figure 7. Sodium transport is influenced by the protonation states in the O-site. (A) Dynamics of Na^+ ions between the O- and N-sites in unbiased MD simulations from the center of the membrane (z = 0 Å) with $Asp37_G$ modeled in deprotonated (blue) and protonated (red) states. The structure depicted in (B) is marked with a yellow circle. (B) Structural snapshot of the sodium motion after 500 ns of classical MD simulation. Intermediate sodium positions during the simulation are marked with dashed circles in the structure and the time trace depicted in panel A. Residues forming contacts with sodium ions during the simulation are listed in black if the ConSurf score is at least eight and otherwise in gray (see Table S4).

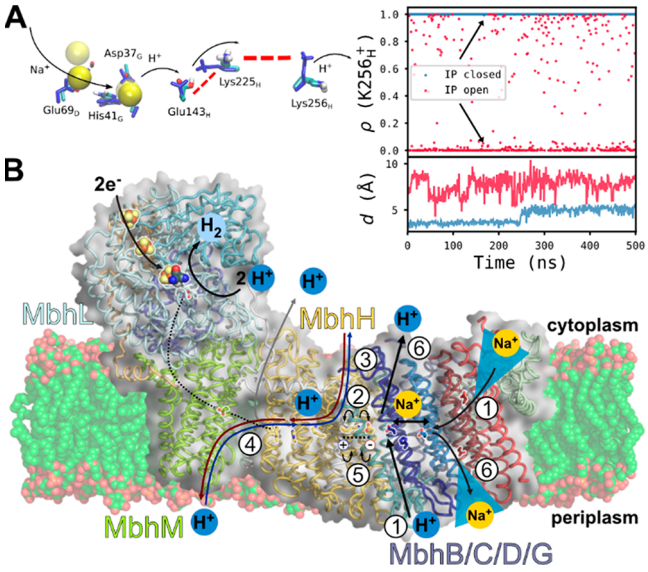

Figure 8. Putative redox-driven Na^+/H^+ transport and proton pumping in Mbh. (A) Sodium binding to the O-site triggers protonation changes, conformational switching of the $Glu143_H$/$Lys225_H$ ion pair and deprotonation of $Lys256_H$. Inset: the predicted protonation fraction of $Lys256_H$ for the open ion pair (blue) and closed ion pair conformations (red). (B) Summary of mechanistic model: (1) Na^+ uptake to the O-site via MbhB/C/D (N-site) and H^+ uptake via MbhB, (2) modulate the conformational state of the buried ion pair in MbhH, and (3) trigger proton transfer across the membrane in MbhH. (4) Reprotonation of $Lys256_H$ induces (5) association of the ion pair and (6) ejection of the Na^+ and H^+ across opposites sides of the membrane. Protonation of the O-site lowers the affinity of the Na^+, which could leave via the P-site by conformational changes in the MbhD gate (see text). Protons could exit to the cytoplasmic side via a water cluster observed in MbhG.

conformational change in the π-bulge region of MbhD-TM3 (Figure S10). Na^+ binding drastically reduces the proton affinity of both $Glu69_D$ and $Asp37_D$, suggesting that the Na^+/H^+ binding events are tightly coupled (Figure S8).

The water network analysis suggests that $Asp37_G$ and $Glu143_H$ are in direct hydrogen-bonded contact via 2−3 water molecules, which could enable proton transfer between the residues upon Na^+ binding. To test this process, we transferred the proton from $Asp37_G$ to $Glu143_H$, which leads to rapid dissociation of $Lys225_H$ toward $Lys256_H$. These conformational changes lower the pK_a of $Lys256_H$ and could thus trigger proton transfer in the MbhH subunit (Figure 8A and Figure S8).

DISCUSSION

Mbh was originally suggested to function as a proton pump based on experiments performed in membrane vesicles.[3] However, it is also possible that the enzyme employs the small energy transduced from Fd-driven hydrogen production to drive secondary active sodium/proton exchange,[4,6] an operational mode that is consistent with the sodium-dependent F_0F_1-ATP synthase in *P. furiosus*.[33] Sodium functions as the coupling ion in the homologous hydrogenase in *Thermococcus onnurineus* NA1, supporting a possible similar role also in Mbh.[34]

Although the exact Na^+/H^+ stoichiometry of Mbh is unknown, the bioenergetic boundary conditions thermodynamically allow Mbh to transfer one ion (Na^+ or H^+) per $2e^-$ at 120 mV sodium motive force (smf) and thus enable the possible electrogenic function of Mbh (cf. also refs 3 and 35). In contrast, for the related Mrps, which lack the redox module, mechanisms based on one Na^+ exchanged per proton[15] or even sodium transport without H^+ exchange were recently suggested.[14]

We propose that the terminal MbhA-MbhG module functions as the sodium translocation domain in Mbh (cf. also refs 1 and 15), whereas the hydration dynamics in MbhH supports its involvement in proton transfer. Our findings indicate that the conserved $Lys225_H/Glu143_H$ ion pair of MbhH and the putative Na^+/H^+ binding O-site establish a coupling element between the proton and sodium transport and proton pumping (Figure 8A). To this end, the sodium affinity at the O-site is modulated by the protonation state of the $Glu69_D/His41_G/Asp37_G$ cluster, and vice versa. Na^+ binding to this site could trigger dissociation of the $Lys225_H/Glu143_H$ ion pair (Figures 7 and 8A) and, in turn, induce proton transfer from $Lys256_H$ (Figure 8A), either directly across the membrane via $His350_H/Lys354_H$ and water molecules around TM7 (Figure 8B) or laterally toward the MbhH/M interface (Figure 8B). However, because the unresolved lipid cleft poses challenges in the current modeling

https://doi.org/10.1021/jacs.1c09356
J. Am. Chem. Soc. 2021, 143, 20873−20883

and the region lacks titratable groups, it remains possible that the MbhH/M interface is not used for proton transfer to the cytoplasmic side. As an alternative, we propose that the protons are taken up via the water-mediated pathway formed along TM12 and transferred via the $Lys409_H$-$His346_H$-$His350_H$ chain to reprotonate $Lys256_H$. This is expected to result in reassociation of the $Lys225_H$/$Glu143_H$ ion pair and ejection of the proton from the O-site to the cytoplasmic side as well as Na^+ ejection to the periplasmic side. The ion release could involve conformational switching into an alternate access state, e.g., at the MbhB/D interface. Conformational changes in MbhD were found to favor Na^+ transfer between the N- and O-sites (Figure S10), whereas the proton release could occur via the water cluster observed at MbhD/G.

In this putative model, the transport of Na^+ and H^+ across the membrane could be triggered by reprotonation of $Lys256_H$ in MbhH, thus following overall similar, although simpler, physical principles as proposed for complex I.[8] Although the exact molecular principles of the redox-driven conformational changes in the conserved loop regions and charge arrays in MbhM and MbhI/L remain unclear, we note that the so-called E-tunnel could regulate the proton affinity and accessibility of the terminal lysine in MbhH and be involved in coupling the redox reactions with the charge transport process.

On the basis of the structural similarity to complex I, we note that the functional elements in MbhH are also expected to support proton conduction in the reverse direction, depending on the external conditions, and therefore do not exclude the possibility of its involvement in establishing a secondary proton gradient (Figure 8B, cf. refs 4 and 6).

Our study also found evidence for proton pathways leading to the NiFe center, with input sites, around the highly conserved $\beta1-\beta2$ loop interface, leading to $Cys374_L$ and the metal bound hydride in the active site via $Glu21_L$. $Glu21_L$ undergoes a protonation-state-dependent conformational switching, which could help shuttle protons to the active site. A similar conformational switching of the functionally central Glu242 in cytochrome *c* oxidase has been suggested to favor kinetic gating and prevent possible back-leaks.[39]

Previous MD simulations on the NiFe-hydrogenase from *D. vulgaris* revealed three proton pathways leading to $Glu34_L$ (equivalent of $Glu21_{MbhL}$),[40] a residue that is also supported by other experimental[41] and computational[30] studies. More specifically, two pathways were observed in NiFe-hydrogenases that correspond to our channels at the MbhL/I/J interface, whereas another pathway showed overall resemblance to our MbhL/N/J channel.[40] To this end, we note that the membrane subunit MbhM could lead to some structural differences at the MbhL/M interface. A pathway resembling the MbhL/M site was also observed in respiratory complex I (Figure S3),[42] whereas hydration through the E-channel from the cleft region in Mbh has not been described before. Interestingly, $His75_{MbhL}$ has also been suggested to form an alternative pathway to the active site.[21,43] Although we find no significant contribution of the latter channel in the modeled states (Figure S3A), our data provide further support for several of the other pathways previously observed in NiFe-hydrogenases.

We note that oxygen sensitivity in hydrogenases has been linked to a proximal 3Fe4S iron sulfur center as well as to the topology of the hydrophobic gas channels leading to the active site.[41,43,44] Mbh shows an oxygen tolerance with a half-life of around 14 h in oxygen sensitivity assays,[6] despite comprising only 4Fe4S centers. Mutational studies suggest that constriction of the hydrophilic tunnel around the corresponding MbhI/J/L pathway observed here can significantly enhance the oxygen tolerance in NiFeSe-hydrogenases from *D. vulgaris*.[45] These findings indicate that the MbhI/J/L pathway could also be relevant for the oxygen tolerance of Mbh, whereas explicit diffusion of O_2 or H_2 along the channels would be necessary to study the effect.

CONCLUSIONS

We have presented here functional dynamics of the membrane-bound hydrogenase (Mbh) from *Pyrococcus furiosus* by using large-scale molecular simulations. In summary, we observed putative water-mediated proton pathways leading along the MbhL/MbhM interface to $Glu21_L$, which could shuttle protons to the NiFe center, responsible for the H_2 production. We also observed significant hydration changes in the MbhH subunit during the MD simulations as well as pK_a shifts upon conformational changes in a buried ion-pair at the MbhH/MbhG interface—functional elements that could support proton transfer across the archaeal membrane. The simulations also revealed three putative Na^+ binding sites that could be responsible for the Na^+/H^+ transport activity of Mbh. The N-site at the MbhC/B interface is a Thr/Ser-rich region, which, via conformational changes in a transmembrane helix of MbhD, can transfer Na^+ ions to the buried carboxylate rich O-site, located at the MbhG/MbhD interface. Conformational switching of an analogous TM-helix was recently suggested to regulate proton transfer also in the canonical complex I[24] (cf. also ref 23). We further found that the Na^+ affinity of the O-site is sensitive to the protonation state of $Asp37_G$, and vice versa. This putative Na^+/H^+ binding site is electrostatically strongly coupled to the buried ion pair at the MbhH/MbhG interface, which in turn could trigger proton transfer along MbhH. We also found evidence for a putative Na^+ binding site at the periplasmic side of the membrane in MbhC/B/F, which upon conformational changes could become accessible to the O-site binding region. Our combined findings provide insight into key conserved coupling principles within the complex I superfamily and detailed functional insight into archaeal energy transduction mechanisms.

MATERIALS AND METHODS

The cryo-EM structure of Mbh from *Pyrococcus furiosus* (PDB ID: 6CFW)[1] was embedded in a 1-palmitoyl-2-palmitoleoyl-*sn*-glycero-3-phosphoinositol (PYPI) membrane by using CHARMM-GUI.[46] We additionally modeled two PYPI lipid molecules in the cleft between MbhH and MbhM, unresolved side chains in MbhI, and missing N/C-terminal residues. The model was embedded in a 200 × 100 × 168 $Å^3$ box comprising TIP3P water molecules and ions to mimic a 250 mM NaCl concentration. MD simulations were performed by using the CHARMM36m force field[47] in combination with force field parameters for the NiFe site for the NIB ($Fe^{II}/Ni^{III}-OH^-$) and NIC ($Fe^{II}/Ni^{III}-H^-$ ligand) states.[48] The MD simulations were performed by using NAMD ver. 2.13[49] with periodic boundary conditions (PBC) and long-range electrostatics modeled with the particle mesh Ewald (PME) approach with a grid size of 1 Å, at 1 bar and 310 K, and with a 2 fs integration time step. The membrane was first equilibrated around the protein, with heavy atoms restrained by a harmonic force constant of 10 kcal mol^{-1} $Å^{-2}$. Lipid tails were initially melted with a harmonic restraint on the headgroups. After gradual heating to 310 K, all restraints were removed, followed by creation of the NIB and NIC states and models with different protonation states of the titratable residues. Initial protonation states were assigned based on electrostatic calculations (see the Supporting Information and Table S2). MDAnalysis,[50] Visual Molecular Dynamics,[51] and PyMol[52] were used

https://doi.org/10.1021/jacs.1c09356
J. Am. Chem. Soc. 2021, 143, 20873−20883

for analysis and visualization (see the Supporting Information Methods and Table S1 for further simulation details).

Clustering Analysis. Hydration dynamics in the MD simulations were analyzed in all states by aligning the trajectories around subunits MbhA-MbhH, MbhI, and MbhM, or MbhJ-MbhN. C_α atoms of residues in helices and sheets were used to define the scope of the analysis by a convex hull. Water molecules around putative sodium sites were identified within 6 Å of the center of mass of the O-site ($E143_H$, $K225_H$, $D37_G$, $H41_G$, $E69_D$), N-site ($D35_B$), or P-site ($D59_B$). For MbhH, water molecules within 4 Å of $K409_H$, $H350_H$, $K354_H$, or $K256_H$, and for the NiFe site, water molecules within 4 Å of $E21_L$ were considered in the analysis. The clustering analysis was performed with Aquaduct ver. 1.0.11[53] using the Barber algorithm (at a cutoff of 1.4 Å), with path trimming for the sodium site analysis. Water analysis was performed on the full data set for all sites in the membrane domain. Water clusters in the active site were analyzed based on simulations S3, S5, S10, and S11 (Table S1). The largest cluster was recursively divided into two subclusters by using the balanced-iterative reducing and clustering using the hierarchies (BIRCH) method for simulations S3 and S10 (for NiFe site) and simulations S1, S3, S4, and S9 (for MbhH). Clusters with <10 members were assigned to the outlier cluster, and conserved residues were identified by using ConSurf.[54] For the visualization of cluster medoid paths, paths with the same input and output cluster were chosen.

DFT Models. Quantum chemical DFT models of the NiFe site were created based on the MD-minimized Mbh model. The DFT model comprised $E21_L$, $C68_L$, $I70_L$, $C71_L$, $H75_L$, $T376_L$, $R320_L$, $D372_L$, $C374_L$, $C377_L$, and $N36_J$, the NiFe core, and three H_2O molecules. Amino acids were cut and saturated with hydrogen atoms at the Cα−Cβ bond. The DFT model comprised 126 atoms, which were structure optimized at the B3LYP-D3/ε=4 level[55,56] by using the def2-SVP basis sets for all atoms except Fe and Ni, which were modeled with the def2-TZVP basis sets.[57] The reaction pathway for proton transfer from $E21_L$ to $C374_L$ and $C374_L$ to H^- were optimized along minimum-energy pathways, followed by optimization of H_3O^+ transition state, which showed one imaginary frequency at −924.6 cm^{-1} (see the Supporting Information Methods). All systems were optimized in the triplet spin state. TURBOMOLE ver. 7.5[58] was used for the DFT calculations (see Supporting Information Methods, Figure S4, and Table S5 for details of all QM calculations).

■ ASSOCIATED CONTENT

Supporting Information

The Supporting Information is available free of charge at https://pubs.acs.org/doi/10.1021/jacs.1c09356.

Figures showing global dynamics, lipid binding, hydration analysis, hydration pathways, ion-pair distance distributions, radial distribution functions, surface contact area and its anticorrelation with O-site hydration, helicity measures, sodium dynamics, QM models, conserved residues, pK_a distributions and simulation details (PDF)

Movie S1 (MPG)

■ AUTHOR INFORMATION

Corresponding Author

Ville R. I. Kaila − *Department of Biochemistry and Biophysics, Stockholm University, 10691 Stockholm, Sweden; Department of Chemistry, Technical University of Munich, 85748 Garching, Germany;* orcid.org/0000-0003-4464-6324; Email: ville.kaila@dbb.su.se

Authors

Max E. Mühlbauer − *Department of Biochemistry and Biophysics, Stockholm University, 10691 Stockholm, Sweden; Department of Chemistry, Technical University of Munich, 85748 Garching, Germany*

Ana P. Gamiz-Hernandez − *Department of Biochemistry and Biophysics, Stockholm University, 10691 Stockholm, Sweden*

Complete contact information is available at: https://pubs.acs.org/10.1021/jacs.1c09356

Notes

The authors declare no competing financial interest.

■ ACKNOWLEDGMENTS

This work was supported the European Research Council (ERC) under the European Union's Horizon 2020 research and innovation program (grant agreement number 715311), the Knut and Alice Wallenberg Foundation, the Swedish Research Council, and the German Research Foundation, TRR235 (Emergence of life). Computing resources were provided by LRZ/SuperMuc (grant: pn34he) and SNIC/PDC (SNIC 2020/1-38) at PDC Centre, partially funded by the Swedish Research Council through grant agreement no. 2016-07213.

■ REFERENCES

(1) Yu, H.; Wu, C.-H.; Schut, G. J.; Haja, D. K.; Zhao, G.; Peters, J. W.; Adams, M. W. W.; Li, H. Structure of an Ancient Respiratory System. *Cell* **2018**, *173*, 1636−1649.

(2) Sapra, R.; Verhagen, M. F.; Adams, M. W. W. Purification and characterization of a membrane-bound hydrogenase from the hyperthermophilic archaeon Pyrococcus furiosus. *J. Bacteriol.* **2000**, *182*, 3423−3428.

(3) Sapra, R.; Bagramyan, K.; Adams, M. W. W. A simple energy-conserving system: proton reduction coupled to proton translocation. *Proc. Natl. Acad. Sci. U. S. A.* **2003**, *100*, 7545−7550.

(4) Schut, G. J.; Boyd, E. S.; Peters, J. W.; Adams, M. W. W. The modular respiratory complexes involved in hydrogen and sulfur metabolism by heterotrophic hyperthermophilic archaea and their evolutionary implications. *FEMS Microbiol. Rev.* **2013**, *37*, 182−203.

(5) Mayer, F.; Müller, V. Adaptations of anaerobic archaea to life under extreme energy limitation. *FEMS Microbiol. Rev.* **2014**, *38*, 449−472.

(6) McTernan, P. M.; Chandrayan, S. K.; Wu, C. H.; Vaccaro, B. J.; Lancaster, W. A.; Yang, Q.; Fu, D.; Hura, G. L.; Tainer, J. A.; Adams, M. W. W. Intact functional fourteen-subunit respiratory membrane-bound [NiFe]-hydrogenase complex of the hyperthermophilic archaeon *Pyrococcus furiosus*. *J. Biol. Chem.* **2014**, *289*, 19364−19372.

(7) Yu, H.; Haja, D. K.; Schut, G. J.; Wu, C. H.; Meng, X.; Zhao, G.; Li, H.; Adams, M. W. W. Structure of the respiratory MBS complex reveals iron-sulfur cluster catalyzed sulfane sulfur reduction in ancient life. *Nat. Commun.* **2020**, *11*, 5953.

(8) Kaila, V. R. I. Long-range proton-coupled electron transfer in biological energy conversion: Towards mechanistic understanding of respiratory complex I. *J. R. Soc., Interface* **2018**, *15*, 20170916.

(9) Sazanov, L. A. A giant molecular proton pump: structure and mechanism of respiratory complex I. *Nat. Rev. Mol. Cell Biol.* **2015**, *16*, 375−388.

(10) Hirst, J. Mitochondrial Complex I. *Annu. Rev. Biochem.* **2013**, *82*, 551−575.

(11) Yu, H.; Schut, G. J.; Haja, D. K.; Adams, M. W. W.; Li, H. Evolution of complex I-like respiratory complexes. *J. Biol. Chem.* **2021**, *296*, 100740.

(12) Kaila, V. R. I.; Wikström, M. Architecture of bacterial respiratory chains. *Nat. Rev. Microbiol.* **2021**, *19*, 319−330.

(13) Lubitz, W.; Ogata, H.; Rüdiger, O.; Reijerse, E. Hydrogenases. *Chem. Rev.* **2014**, *114*, 4081−4148.

(14) Li, B.; Zhang, K.; Nie, Y.; Wang, X.; Zhao, Y.; Zhang, X. C.; Wu, X. L. Structure of the *Dietzia* Mrp complex reveals molecular

mechanism of this giant bacterial sodium proton pump. *Proc. Natl. Acad. Sci. U. S. A.* **2020**, *117*, 31166−31176.
(15) Steiner, J.; Sazanov, L. Structure and mechanism of the Mrp complex, an ancient cation/proton antiporter. *eLife* **2020**, *9*, e59407.
(16) Di Luca, A.; Gamiz-Hernandez, A. P.; Kaila, V. R. I. Symmetry-related proton transfer pathways in respiratory complex I. *Proc. Natl. Acad. Sci. U. S. A.* **2017**, *114*, E6314−E6321.
(17) Kaila, V. R. I.; Wikström, M.; Hummer, G. Electrostatics, hydration, and proton transfer dynamics in the membrane domain of respiratory complex I. *Proc. Natl. Acad. Sci. U. S. A.* **2014**, *111*, 6988−6993.
(18) Baradaran, R.; Berrisford, J. M.; Minhas, G. S.; Sazanov, L. A. Crystal structure of the entire respiratory complex I. *Nature* **2013**, *494*, 443−448.
(19) Mühlbauer, M. E.; Saura, P.; Nuber, F.; Di Luca, A.; Friedrich, T.; Kaila, V. R. I. Water-gated proton transfer dynamics in respiratory complex I. *J. Am. Chem. Soc.* **2020**, *142*, 13718−13728.
(20) Röpke, M.; Saura, P.; Riepl, D.; Pöverlein, M. C.; Kaila, V. R. I. Functional Water Wires Catalyze Long-Range Proton Pumping in the Mammalian Respiratory Complex I. *J. Am. Chem. Soc.* **2020**, *142*, 21758−21766.
(21) Grba, D. N.; Hirst, J. Mitochondrial complex I structure reveals ordered water molecules for catalysis and proton translocation. *Nat. Struct. Mol. Biol.* **2020**, *27*, 892−900.
(22) Zickermann, V.; Wirth, C.; Nasiri, H.; Siegmund, K.; Schwalbe, H.; Hunte, C.; Brandt, U. Mechanistic insight from the crystal structure of mitochondrial complex I. *Science* **2015**, *347*, 44−49.
(23) Kampjut, D.; Sazanov, L. A. The coupling mechanism of mammalian respiratory complex I. *Science* **2020**, *370*, eabc4209.
(24) Röpke, M.; Riepl, D.; Saura, P.; Di Luca, A.; Mühlbauer, M. E.; Jussupow, A.; Gamiz-Hernandez, A. P.; Kaila, V. R. I. Deactivation blocks proton pathways in the mitochondrial complex I. *Proc. Natl. Acad. Sci. U. S. A.* **2021**, *118*, e2019498118.
(25) Di Luca, A.; Kaila, V. R. I. Molecular strain in the active/deactive-transition modulates domain coupling in respiratory complex I. *Biochim. Biophys. Acta, Bioenerg.* **2021**, *1862*, 148382.
(26) Agip, A. N. A.; Blaza, J. N.; Bridges, H. R.; Viscomi, C.; Rawson, S.; Muench, S. P.; Hirst, J. Cryo-EM structures of complex I from mouse heart Mitochondria in two Biochemically Defined States. *Nat. Struct. Mol. Biol.* **2018**, *25*, 548−556.
(27) Fiedorczuk, K.; Letts, J. A.; Degliesposti, G.; Kaszuba, K.; Skehel, M.; Sazanov, L. A. Atomic structure of the entire mammalian mitochondrial complex I. *Nature* **2016**, *538*, 406−410.
(28) Lobasso, S.; Lopalco, P.; Angelini, R.; Vitale, R.; Huber, H.; Müller, V.; Corcelli, A. Coupled TLC and MALDI-TOF/MS analyses of the lipid extract of the hyperthermophilic archaeon *Pyrococcus furiosus*. *Archaea* **2012**, *2012*, 957852.
(29) Siegbahn, P. E. M.; Liao, R. Z. The Energetics of Hydrogen Molecule Oxidation in NiFe-hydrogenase. *ACS Catal.* **2020**, *10*, 5603−5613.
(30) Siegbahn, P. E. M.; Tye, J. W.; Hall, M. B. Computational studies of [NiFe] and [FeFe] hydrogenases. *Chem. Rev.* **2007**, *107*, 4414−4135.
(31) Rich, P. R.; Maréchal, A. Functions of the hydrophilic channels in protonmotive cytochrome c oxidase. *J. R. Soc., Interface* **2013**, *10*, 20130183.
(32) Suomivuori, C. M.; Gamiz-Hernandez, A. P.; Sundholm, D.; Kaila, V. R. I. Energetics and dynamics of a light-driven sodium-pumping rhodopsin. *Proc. Natl. Acad. Sci. U. S. A.* **2017**, *114*, 7043−7048.
(33) Pisa, K. Y.; Huber, H.; Thomm, M.; Müller, V. A sodium ion-dependent A1AO ATP synthase from the hyperthermophilic archaeon Pyrococcus furiosus. *FEBS J.* **2007**, *274*, 3928−3938.
(34) Lim, J. K.; Mayer, F.; Kang, S. G.; Müller, V. Energy conservation by oxidation of formate to carbon dioxide and hydrogen via a sodium current in a hyperthermophilic archaeon. *Proc. Natl. Acad. Sci. U. S. A.* **2014**, *111*, 11497−502.
(35) Calisto, F.; Sousa, F. M.; Sena, F. V.; Refojo, P. N.; Pereira, M. M. Mechanisms of Energy Transduction by Charge Translocating Membrane Proteins. *Chem. Rev.* **2021**, *121*, 1804−1844.
(36) Haapanen, O.; Sharma, V. Role of water and protein dynamics in proton pumping by respiratory complex I. *Sci. Rep.* **2017**, *7*, 7747.
(37) Jardetzky, O. Simple Allosteric Model for Membrane Pumps. *Nature* **1966**, *211*, 969−970.
(38) Forrest, L. R.; Zhang, Y.; Jacobs, M. T.; Gesmonde, J.; Xie, L.; Honig, B. H.; Rudnick, G. Mechanism for alternating access in neurotransmitter transporters. *Proc. Natl. Acad. Sci. U. S. A.* **2008**, *105*, 10338−10343.
(39) Kaila, V. R. I.; Verkhovsky, M. I.; Hummer, G.; Wikström, M. Glutamic acid 242 is a valve in the proton pump of cytochrome c oxidase. *Proc. Natl. Acad. Sci. U. S. A.* **2008**, *105*, 6255−6259.
(40) Sumner, I.; Voth, G. A. Proton Transport Pathways in [NiFe]-Hydrogenase. *J. Phys. Chem. B* **2012**, *116*, 2917−2926.
(41) Tai, H.; Hirota, S.; Stripp, S. T. Proton Transfer Mechanisms in Bimetallic Hydrogenases. *Acc. Chem. Res.* **2021**, *54*, 232−241.
(42) Jussupow, A.; Di Luca, A.; Kaila, V. R. I. How cardiolipin modulates the dynamics of respiratory complex I. *Sci. Adv.* **2019**, *5* (3), 1850.
(43) Fontecilla-Camps, J. C.; Volbeda, A.; Cavazza, C.; Nicolet, Y. Structure/Function Relationships of [NiFe]- and [FeFe]-Hydrogenases. *Chem. Rev.* **2007**, *107*, 4273−4303.
(44) Kalms, J.; Schmidt, A.; Frielingsdorf, S.; Utesch, T.; Gotthard, G.; von Stetten, D.; van der Linden, P.; Royant, A.; Mroginski, M. A.; Carpentier, P.; Lenz, O.; Scheerer, P. Tracking the Route of Molecular Oxygen in O2-Tolerant Membrane-Bound [NiFe] Hydrogenase. *Proc. Natl. Acad. Sci. U. S. A.* **2018**, *115*, E2229−E2237.
(45) Zacarias, S.; Temporão, A.; del Barrio, M.; Fourmond, V.; Léger, C.; Matias, P. M.; Pereira, I. A. C. A Hydrophilic Channel Is Involved in Oxidative Inactivation of a [NiFeSe] Hydrogenase. *ACS Catal.* **2019**, *9*, 8509−8519.
(46) Jo, S.; Kim, T.; Iyer, V. G.; Im, W. CHARMM-GUI: A Web-based Graphical User Interface for CHARMM. *J. Comput. Chem.* **2008**, *29*, 1859−1865.
(47) Best, R. B.; Zhu, X.; Shim, J.; Lopes, P. E. M.; Mittal, J.; Feig, M.; Mackerell, A. D., Jr. Optimization of the additive CHARMM all-atom protein force field targeting improved sampling of the backbone φ, ψ and side-chain χ_1 and χ_2 dihedral angles. *J. Chem. Theory Comput.* **2012**, *8*, 3257−3273.
(48) Smith, D. M.; Xiong, Y.; Straatsma, T. P.; Rosso, K. M.; Squier, T. C. Force-Field Development and Molecular Dynamics of [NiFe] Hydrogenase. *J. Chem. Theory Comput.* **2012**, *8*, 2103−2114.
(49) Phillips, J. C.; Braun, R.; Wang, W.; Gumbart, J.; Tajkhorshid, E.; Villa, E.; Chipot, C.; Skeel, R. D.; Kalé, L.; Schulten, K. Scalable molecular dynamics with NAMD. *J. Comput. Chem.* **2005**, *26*, 1781−1802.
(50) Michaud-Agrawal, N.; Denning, E. J.; Woolf, T. B.; Beckstein, O. MDAnalysis: A Toolkit for the Analysis of Molecular Dynamics Simulations. *J. Comput. Chem.* **2011**, *32*, 2319−2327.
(51) Humphrey, W. A.; Dalke, A.; Schulten, K. VMD: Visual molecular dynamics. *J. Mol. Graphics* **1996**, *14*, 33−38.
(52) Delano, W. L. The PyMOL Molecular Graphics System, ver. 2.5; https://pymol.org/2/ (accessed 2021-10-29).
(53) Magdziarz, T.; Mitusińska, K.; Bzówka, M.; Raczyńska, A.; Stańczak, A.; Banas, M.; Bagrowska, W.; Góra, A. AQUA-DUCT 1.0: structural and functional analysis of macromolecules from an intramolecular voids perspective. *Bioinformatics* **2020**, *36*, 2599−2601.
(54) Ashkenazy, H.; Abadi, S.; Martz, E.; Chay, O.; Mayrose, I.; Pupko, T.; Ben-Tal, N. ConSurf 2016: an improved methodology to estimate and visualize evolutionary conservation in macromolecules. *Nucleic Acids Res.* **2016**, *44*, W344−W350.
(55) Becke, A. D. Density-functional thermochemistry. III. The role of exact exchange. *J. Chem. Phys.* **1993**, *98*, 5648−5652.
(56) Grimme, S.; Antony, J.; Ehrlich, S.; Krieg, H. A. Consistent and accurate ab initio parametrization of density functional dispersion correction (DFT-D) for the 94 elements H-Pu. *J. Chem. Phys.* **2010**, *132*, 154104−19.

https://doi.org/10.1021/jacs.1c09356
J. Am. Chem. Soc. 2021, 143, 20873−20883

(57) Schäfer, A.; Horn, H.; Ahlrichs, R. Fully optimized contracted Gaussian basis sets for atoms Li to Kr. *J. Chem. Phys.* **1992**, *97*, 2571−2577.
(58) Ahlrichs, R.; Bär, M.; Häser, M.; Horn, H.; Kölmel, C. Electronic structure calculations on workstation computers: The program system turbomole. *Chem. Phys. Lett.* **1989**, *162*, 165−169.

https://doi.org/10.1021/jacs.1c09356
J. Am. Chem. Soc. 2021, 143, 20873−20883